A SINFONI integral field spectroscopy survey for galaxy counterparts to damped Lyman a systems - VI. Metallicity and geometry as gas flow probes

Celine Peroux, Samuel Quiret, Hadi Rahmani, Varsha P. Kulkarni, Benoit Epinat, Bruno Milliard, Lorrie A. Straka, Donald G. York, Alireza Rahmati, Thierry Contini

Monthly Notices
of the
ROYAL ASTRONOMICAL SOCIETY
MNRAS **457,** 903–916 (2016) doi:10.1093/mnras/stw016

A SINFONI integral field spectroscopy survey for galaxy counterparts to damped Lyman α systems – VI. Metallicity and geometry as gas flow probes⋆

Céline Péroux,[1]† Samuel Quiret,[1] Hadi Rahmani,[1] Varsha P. Kulkarni,[2] Benoit Epinat,[1] Bruno Milliard,[1] Lorrie A. Straka,[3] Donald G. York,[4] Alireza Rahmati[5] and Thierry Contini[6]

[1]*Aix Marseille Université, CNRS, LAM (Laboratoire d'Astrophysique de Marseille) UMR 7326, F-13388 Marseille, France*
[2]*Department of Physics and Astronomy, Univ. of South Carolina, Columbia, SC 29208, USA*
[3]*Sterrewacht Leiden, Leiden University, PO Box 9513, NL-2300 RA Leiden, the Netherlands*
[4]*Department of Astronomy and Astrophysics and The Enrico Fermi Institute, University of Chicago, 5640 S. Ellis Ave, Chicago, IL 60637, USA*
[5]*Institute for Computational Science, University of Zürich, Winterthurerstrasse 190, CH-8057 Zürich, Switzerland*
[6]*IRAP, Institut de Recherche en Astrophysique et Planétologie, CNRS, 14, avenue Edouard Belin, F-31400 Toulouse, France; Université de Toulouse, UPS-OMP, F-31400 Toulouse, France*

Accepted 2016 January 1. Received 2015 December 21; in original form 2015 August 4

ABSTRACT

The use of background quasars provides a powerful tool to probe the cool gas in the circumgalactic medium of foreground galaxies. Here, we present new observations with SINFONI and X-Shooter of absorbing-galaxy candidates at $z = 0.7$–1. We report the detection with both instruments of the Hα emission line of one sub-damped Lyman α (sub-DLA) at $z_{\rm abs} = 0.941\,87$ with $\log N({\rm H\,I}) = 19.38^{+0.10}_{-0.15}$ towards SDSS J002133.27+004300.9. We estimate the star formation rate: SFR $= 3.6 \pm 2.2$ M$_\odot$ yr^{-1} in that system. A detailed kinematic study indicates a dynamical mass $M_{\rm dyn} = 10^{9.9\pm0.4}$ M$_\odot$ and a halo mass $M_{\rm halo} = 10^{11.9\pm0.5}$ M$_\odot$. In addition, we report the [O II] detection with X-Shooter of another DLA at $z_{\rm abs} = 0.7402$ with $\log N({\rm H\,I}) = 20.4 \pm 0.1$ towards Q0052+0041 and an estimated SFR of 5.3 ± 0.7 M$_\odot$ yr^{-1}. Three other objects are detected in the continuum with X-Shooter but the nature and redshift of two of these objects are unconstrained due to the absence of emission lines, while the third object might be at the redshift of the quasar. We use the objects detected in our whole N(H I)-selected SINFONI survey to compute the metallicity difference between the galaxy and the absorbing gas, $\delta_{\rm H\,I}(X)$, where a positive (negative) value indicates infall (outflow). We compare this quantity with the quasar line-of-sight alignment with the galaxy's major (minor) axis, another tracer of infall (outflow). We find that these quantities do not correlate as expected from simple assumptions. Additional observations are necessary to relate these two independent probes of gas flows around galaxies.

Key words: galaxies: abundances – galaxies: evolution – galaxies: formation – intergalactic medium – galaxies: ISM – quasars: absorption lines.

1 INTRODUCTION

While the large-scale intergalactic medium (IGM) and small-scale processes within the galaxies are now better understood, the next challenge to probe the history of baryons is to focus on the circumgalactic medium (CGM), a gas-rich region which lies around galaxies but inside their dark matter haloes, at scales between 10–20 kpc (galaxy's radius) and 100–200 kpc (dark matter halo virial radius). In particular, the interactions between gas inflows (imposed by large-scale dark matter structures from IGM reservoirs) and outflows (launched by star-forming regions in galaxies and active supermassive black holes) are of paramount importance.

Outflows are commonly probed by the presence of interstellar absorption lines from cool gas superimposed on the stellar

⋆ Based on observations collected during programmes ESO 078.A-0003, 092.A-0167 and 095.A-0338 at the European Southern Observatory with UVES, SINFONI and X-Shooter on the 8.2 m telescopes operated at the Paranal Observatory, Chile.

†E-mail: celine.peroux@gmail.com

continuum which are blueshifted by hundreds of km s^{-1} relative to the background galaxies' systemic velocities (Shapley et al. 2003; Steidel et al. 2010). Strong Mg II absorbers in particular (Tremonti, Moustakas & Diamond-Stanic 2007; Martin & Bouché 2009; Martin et al. 2012; Schroetter et al. 2015) have been observed to extend out to 100 kpc along the galaxies' minor axes (Bordoloi et al. 2011). Outflows are ubiquitous in galaxies at various redshifts (e.g. Pettini et al. 2001; Steidel, Pettini & Adelberger 2001; Martin 2005; Rupke, Veilleux & Sanders 2005; Veilleux, Cecil & Bland-Hawthorn 2005; Tremonti et al. 2007; Weiner et al. 2009). Interestingly, the circumgalactic gas has also been probed in emission by Steidel et al. (2011) who stacked narrow-band images of $z \sim 2$–3 galaxies and reveal diffuse Lyα haloes extending to ∼80 kpc. However, given the unknown ionization state and number of phases in the gas, it is at present very difficult to measure the mass in these outflows (e.g. Genzel et al. 2010; Martin et al. 2013). Moreover, galaxies are believed to interact with the IGM by filling it with ionizing photons and by injecting heavy elements formed in stars and supernovae (SNe) through these supersonic galactic winds. Indeed, observations of the IGM indicate significant quantities of metals at all redshifts (Pettini 2003; Ryan-Weber et al. 2009; Tumlinson et al. 2011; Cooksey et al. 2013; Werk et al. 2013; Shull, Danforth & Tilton 2014). The presence of these metals is interpreted as a signature of strong galactic outflows in various models (Aguirre et al. 2001; Oppenheimer & Davé 2006; Pieri, Martel & Grenon 2007).

While observational evidence for outflows is growing, direct probes of infall are notoriously more difficult to gather. Nevertheless, cool gas inflows have recently been detected in a few objects (Sato et al. 2009; Martin et al. 2012; Bouché et al. 2013; Diamond-Stanic et al. 2015). Moreover, accretion is required to explain some of the basic observed properties of galaxies including the gas-phase metallicity (e.g. Erb et al. 2006) and the cosmological evolution of neutral gas mass (Zafar et al. 2013). From a theoretical viewpoint, baryonic infall along the cosmic web on to dark haloes is relatively well understood in Λ cold dark matter models.

The spectra of background quasars provide a powerful tool to probe the cool gas in the CGM. The quasar absorbers, which trace the diffuse gas environment surrounding galaxies, are used to study the CGM of galaxies (Stewart et al. 2011; Rudie et al. 2012; Stinson et al. 2012). However, studying the stellar content of these systems has proved to be very challenging. It is critical to select the rare quasar–galaxy pairs. In recent studies, we have used sightlines selected by their large neutral gas content, damped Lyman α: DLA ($\log N(\mathrm{H\,I}) > 20.3$) and sub-DLA ($19.0 < \log N(\mathrm{H\,I}) < 20.3$) systems at $z \sim 1$ and $z \sim 2$ (Péroux et al. 2011a,b, 2012). Similarly, a sample of Mg II absorbers was used to study winds and infall near galaxies at $z \sim 1$ and $z \sim 2$ (Bouché et al. 2007, 2013; Schroetter et al. 2015), up to a redshift close to the peak of cosmic star formation activity. In these studies, we made use of the advantages afforded by the 3D spectroscopy at near-infrared (NIR) wavelengths made possible by the SINFONI instrument on the European Very Large Telescopes (VLT) aided with the adaptive optics (AO) system to search for and study absorbing galaxies.

The present paper is structured as follows. A summary of observational details and data reduction steps are provided in Section 2. In Section 3, we report the detections of the absorbing galaxies with these new data. Finally, the results for the full $N(\mathrm{H\,I})$-selected sample are presented in Section 4. Throughout this paper, we assume a cosmology with $H_0 = 71$ km s^{-1} Mpc^{-1}, $\Omega_\mathrm{M} = 0.27$ and $\Omega_\Lambda = 0.73$.

2 THE DATA

2.1 Target selection

The target selection in this study differs from previous work by our group (Bouché et al. 2007; Péroux et al. 2011a, 2013; Schroetter et al. 2015). Previously, we performed blind search for emission at the redshift of the quasar absorber. In this case, we select absorbing-galaxy candidates in the quasar field with a known sky position. The candidates are identified based on either a proximity argument (i.e. small impact parameter to the quasar line of sight), a photometric redshift, or a spectroscopic redshift. We emphasize that this is *not* a blind search, but a set of eight $z \sim 1$ quasar/absorbing galaxies matched pairs identified by other studies. We collect from the available literature absorbers with known column density in neutral hydrogen, $N(\mathrm{H\,I})$, with galaxy counterparts identified from either broad-band imaging (Le Brun et al. 1997; Meiring et al. 2011), with photometric redshifts (Rao et al. 2011) or with redshifts confirmed by low-resolution spectroscopy (Lacey et al. 2003). We carefully select objects with redshift so that the λ_obs of Hα emission falls away from OH sky lines.

The neutral gas column density for these systems has been measured from *Hubble Space Telescope* (*HST*)/Faint Object Spectrograph or *HST*/Space Telescope Imaging Spectrograph spectra. We originally requested nine targets to be observed with SINFONI and eight with X-Shooter. A ninth object (J0138−005) has a UVES quasar spectrum available in the archives, so no further observations are needed. In the end, the SINFONI and X-Shooter targets do not exactly overlap due to the fact that our programme is not complete: one field was observed with X-Shooter but not with SINFONI (SDSS J122836.8+101841.7). Finally, one field was not observed with either SINFONI or X-Shooter. Table 1 provides a summary of some of the properties of these targets, including the coordinates of the quasar in the field, quasar magnitude and redshift, absorber redshift, $N(\mathrm{H\,I})$ column density, angular separation between the quasar and the absorbing galaxy for each of the objects and which instrument the field is observed with.

2.2 Observations and data reduction

2.2.1 SINFONI

Unlike in our previous studies with SINFONI (Péroux et al. 2011a, 2012), these new observations are centred on the absorbing galaxy with known sky position. The observations were carried out in service mode (under programme ESO 92.A-0167 A) at the European Southern Observatory (ESO) with SINFONI on the 8.2 m Yepun telescope. The redshifted Hα line lies in the *J* band for these targets at $z \sim 1$. The data are 8 arcsec × 8 arcsec field of view, corresponding to a 0.25 arcsec pixel scale. In order to avoid sky exposures, we nod around the target. The resulting cubes (a mosaic of the 8 arcsec × 8 arcsec SINFONI field of view resulting in an ∼11 arcsec × 11 arcsec effective field of view) are centred on the absorbing galaxy with known sky positions. For two fields where the quasar itself is bright enough, we use it as a natural guide star (NGS) for AO in order to improve the spatial resolution. For the other fields, the data are taken with natural seeing (no AO). The seeing is measured from the quasar in the data cube if present. For two fields, the quasar is not covered. The resulting point spread function (PSF) is fairly poor with full width at half-maximum (FWHM) ranging from 0.70 to 0.95 arcsec. In fact, a number of observing blocks (OBs) are classified as 'executed', i.e. the observations are

Table 1. Targets list. Summary of some of the properties of the quasar field, absorber and absorbing galaxy. The magnitudes are AB magnitudes and the angular separations are referred to as '*b*'.

Quasar[a]	Coordinates[a]	*V* mag	z_{quasar}	z_{abs}	N(H I)	*b* (arcsec)	*b* (kpc)	Inst.
SDSS J002133.27+004300.9	00 21 33.28+00 43 00.99	18.2	1.244	0.9420	$19.38^{+0.10}_{-0.15}$	10.8	86	SINFO/XSH/UVES
Q0052+0041	00 51 30.49+00 41 50.06	18.5	1.19	0.7402	20.4 ± 0.1	3.3	24	SINFO/XSH
SDSS J011615.51−004334.7	01 16 15.52-00 43 34.747	18.7	1.275	0.9127	$19.95^{+0.05}_{-0.11}$	8.1	64	SINFO/XSH
J0138−0005	01 38 25.54-00 05 34.52	18.8	1.340	0.7820	$19.81^{+0.06}_{-0.11}$	6.5	49	SINFO
J045647.17+040052.9	04 56 47.18+04 00 52.94	16.5	1.345	0.8596	20.75 ± 0.03	0.8	14	SINFO/XSH
Q0826−2230	08 26 01.58-22 30 27.20	16.2	0.910	0.9110	19.04 ± 0.04	5.0	40	SINFO/XSH
SDSS J122836.8+101841.7	12 28 36.88+10 18 41.92	18.5	2.306	0.9376	$19.41^{+0.12}_{-0.18}$	4.6	37	XSH
SDSS J152102.00−000903.1	15 21 02.01-00 09 03.21	18.5	2.032	0.9510	$19.40^{+0.08}_{-0.14}$	8.5	68	SINFO/XSH

Note. [a]SIMBAD coordinates unless the quasars is part of SDSS, in which case SDSS names are provided.

Table 2. Journal of high-resolution SINFONI observations. The data are the *J* band and 8 arcsec × 8 arcsec field of view, corresponding to a 0.25 arcsec pixel scale.

Quasar	Observing date	T_{exp}[s] × N_{exp}[a]	AO[b]	PSF[c] (arcsec)
SDSS J002133.27+004300.9	2013 Oct 7	(600 × 4) × (0+1)	No AO	0.75
Q0052+0041	2013 Nov 7	(600 × 4) × (2+0)	No AO	0.95
SDSS J011615.51−004334.7	2013 Oct 5/6	(600 × 4) × (1+1)	No AO	–
J0138−0005	2013 Oct 30/Nov 9	(600 × 4) × (2+0)	No AO	0.75
J045647.17+040052.9	2013 Dec 27	(600 × 4) × (0+2)	NGS	0.90
Q0826−2230	2013 Dec 14/Dec 30	(600 × 4) × (2+0)	NGS	0.70
SDSS J152102.00−000903.1	2014 Mar 22	(600 × 4) × (1+0)	No AO	–

Notes. [a]The two numbers for N_{exp} in parentheses refer to exposures classified as 'completed' and 'executed' (i.e. not within the user specifications in ESO terminology), respectively.
[b]No AO: no adaptive optics, natural seeing. NGS: the quasar is used as a natural guide star for adaptive optics.
[c]The seeing is measured from the quasar in the data cube. For two fields, the quasar is not covered. We note that during the exposure of SDSS J002133.27+004300.9, the seeing degraded to 0.95 arcsec so that the OB is not considered complete by ESO.

taken but not validated as up to ESO standards. The *J*-band grism provides a spectral resolution of around $R \sim 2000$. A journal of observations summarizing the target properties and experimental set-up is presented in Table 2. The table provides the observing date, exposure time, AO system used and the resulting PSF of the combined data.

The data are reduced with the latest version of the ESO SINFONI pipeline (version 2.5.2) and custom routines. The latter are used to correct the raw cubes for bad detector columns and to remove cosmic rays by applying the Laplacian edge technique of van Dokkum (2001). Master bias and flat images based on calibration cubes taken closest in time to the science frames are used to correct each data cube. Bias and flat-field corrections are done within the ESO pipeline. The OH line suppression and sky subtraction are accomplished with additional purpose-developed codes. Within one OB, the science frames are pair-subtracted with an ON–OFF pattern to eliminate variation in the NIR sky background. The wavelength calibration is based on the Ar lamp and is accurate to about ~ 30 km s^{-1} in the *J* band, i.e. comparable with the calculated heliocentric correction (of the order of 10–30 km s^{-1}). For each set of observations, a flux standard star is observed at approximately the same time and at similar airmass as used for the target fields. The flux standard star data are reduced in the same way as the science data. These standard stars are then used for flux calibration by fitting a blackbody spectrum to the O/B stars or a power law to the cool stars ($T < 10\,000$ K) and normalizing them to the 2MASS magnitudes. These spectra are also used to remove atmospheric absorption features from the science cubes. When a quasar is included in the cube, the resulting flux calibration is compared with the quasar 2MASS magnitudes in order to estimate the flux uncertainties. The different observations from the independent OBs are then combined spatially using the position of the quasar in each frame or the PSF calibrator (a bright PSF star), resulting in an average co-added cube for each target.

2.2.2 *X-Shooter*

Seven of the nine targets initially planned are observed with X-Shooter. The observations are carried out in service mode at the ESO with X-Shooter (Vernet et al. 2011) on the 8.2 m Kueyen telescope. Most of the observations are taken under programme ESO 92.A-0167 B, while the object we detect, SDSS J002133.27+004300.9, is re-observed in ESO 095.A-0338 B. The medium-resolution X-Shooter spectrograph covers the full wavelength range from 300 nm to 2.5 μm thanks to the simultaneous use of three spectroscopic arms (UVB, VIS and NIR). Our observing strategy consists of aligning the slit on both the bright background quasar and the faint absorbing galaxy for which the exact sky positions are known from previous publications. In one case (SDSS J002133.27+004300.9), the angular separation is larger than the slit length (11 arcsec) plus nodding length, so that only the absorbing galaxy is observed. We used the long-slit mode with slit width of 1.0 arcsec for UVB

Table 3. Journal of X-Shooter observations. The medium-resolution X-Shooter spectrograph covers the full wavelength range from 300 nm to 2.5 μm. Our observing strategy consists in aligning the slit on both the bright background quasar and the faint absorbing galaxy for which the exact sky positions are known from previous observations, except in one case where the angular separation is larger than the slit length (SDSS J002133.27+004300.9).

Quasar	Observing date	$T_{exp} \times N_{exp}$ (s)	Quasar?	Nodding mode	Nodding length (arcsec)
SDSS J002133.27+004300.9	2013 Nov 17/Dec 16+2015 Jul 2	(1200 × 2+1200 × 2)	n	AutoNod	5
Q0052+0041	2013 Oct 13-21-23/Nov 21	(1440 × 2+1200 × 1)	y	GenericOffset	6
SDSS J011615.51−004334.7	2013 Oct 13/Nov 21	(1200 × 2)	y	GenericOffset	2
J045647.17+040052.9	2013 Dec 5-11-21-22-24	(1440 × 6+1200 × 1)	y	AutoNod	5
Q0826−2230	2013 Dec 12-15-24/Jan 8-19	(1200 × 3)	y	GenericOffset	3
SDSS J122836.8+101841.7	2014 Feb 13-22/Mar 7-12	(1200 × 3)	y	GenericOffset	3
SDSS J152102.00−000903.1	2014 Mar 16	(1200 × 1)	y	GenericOffset	2

and 0.9 arcsec for the VIS and NIR arms. With these settings, the expected spectral resolution is 59 km s^{-1} (UVB), 34 km s^{-1} (VIS) and 53 km s^{-1} (NIR), respectively. Our actual resolution is only slightly higher than these estimates because the typical seeing (0.8 arcsec) is only slightly smaller than the slit widths. To optimize the sky subtraction in the NIR, the nodding mode is used following an ABBA scheme. The nodding length is chosen to avoid both the quasar trace and quasar counter-images falling at the absorbing-galaxy position. As a result, the 'AutoNod' mode is used when a nodding length of 5 arcsec is suitable and fine-tuned otherwise using the 'GenericOffset' mode. The total exposure time is divided into OBs of 1200 or 1440 s each. A journal of observations summarizing the target properties and experimental set-up is presented in Table 3. The table provides the observing date, exposure times, whether the quasar is covered by the slit or not and the nodding mode for each of the fields.

The data are reduced with the latest version (2.6.0) of the ESO X-Shooter pipeline first described in Goldoni et al. (2006) and additional external routines for the extraction of the 1D spectra and their combination. Master bias and flat images based on data taken closest in time to the science frames are used to correct each raw spectrum. Bias and flat-field correction are part of the ESO pipeline. Cosmic rays are removed by applying the Laplacian edge technique of van Dokkum (2001), and sky emission lines are subtracted using the Kelson (2003) method. The orders for each arm are then extracted and rectified in wavelength space using a wavelength solution previously obtained from calibration frames. The 2D orders are merged using the errors as a weight in the overlapping regions. We find that the 1D extraction from the ESO pipeline produces noisy data and choose to perform our own extractions using the '*apall*' routine within IRAF and interactively optimizing the signal window definition and background regions for subtraction.

Based on our experience, removing the quasar trace matters mostly when the angular separation with the target is less than 2 arcsec. For this data sample, in the case of J045647.17+040052.9, the angular separation is small (b = 0.8 arcsec) and requires a particular treatment. Similarly, in two cases (Q0826−2230 and SDSS J122836.8+101841.7), the quasar counter-image is ∼2 arcsec away from the targeted absorbing galaxy. In these cases, we perform a spectral PSF fit to remove the trace from the bright quasar. Details of the method are provided in Rahmani et al. (in preparation), but in short, the quasar is fitted with a Moffat function at each wavelength, except in a small window where emission lines from the faint galaxies are expected. In these regions, the profile is interpolated from either edge. We note in addition that this technique allows one to search for faint absorbing galaxies in exposures where the bright quasar imposes too high a contrast. Finally, for each exposure, we extract a quasar spectrum and, when detected, a spectrum of the absorbing galaxy. We correct the wavelength calibration to a vacuum heliocentric reference. We then merge the 1D spectra weighting each spectrum by the signal-to-noise ratio (SNR).

The spectra were flux-calibrated using a spectrophotometric standard star. In some cases, the NIR and UVB spectrum is scaled to the VIS spectrum to match in the overlapping regions. We calculate that the corrections for slit losses are negligible for these observations. We also note that X-Shooter was not designed nor is it operated in purely photometric conditions. For these reasons, the flux calibration is mostly used to remove instrumental effects.

3 ANALYSIS

3.1 SINFONI detection

We report just one detection with SINFONI in the line of sight towards the quasar SDSS J002133.27+004300.9. The remaining fields do not show Hα at the expected redshifted wavelength even though the galaxies associated with the quasar absorbers were reported in the literature based on photometric or spectroscopic redshift. Note that the SINFONI instrument is not sensitive to continuum detection. References to previous reports in the literature for these absorbing galaxies are provided in the last column of Table 4. The low detection rate is unexpected from a sample selected on the basis of a priori galaxy identification given that spatial coincidences are too rare unless there is some physical connection. We emphasize that these non-detections are genuine, probably indicating a lower star formation rate (SFR) in these objects than our detection limits and possibly high dust attenuation. The limits on the SFR from the Hα non-detection are also provided in Table 4, overall reaching a threshold below <1 M$_\odot$ yr^{-1}.

In the case of the quasar SDSS J002133.27+004300.9 at z_{quasar} = 1.245, Rao, Turnshek & Nestor (2006) have reported two sub-DLAs. One system at z_{abs} = 0.5023 has a column density of $\log N(\mathrm{H\,I}) = 19.54^{+0.02}_{-0.03}$ and another at higher redshift z_{abs} = 0.9420 with $\log N(\mathrm{H\,I}) = 19.38^{+0.10}_{-0.15}$. Furthermore, Rao et al. (2011) have obtained J-, H- and K-band ground-based imaging of 10 × 10 arcsec of this field. After performing a careful PSF subtraction of the quasar, these authors detect no object at small impact parameters. However, three objects are detected further out, two of which are seen in all three bands. Based on both these IR images and Sloan Digital Sky Survey (SDSS) photometry, the so-called 'object 1' was estimated to be at z_{phot} = 0.549 with an $E(B-V)$ = 0.50 and a metallicity Z = 0.004, consistent with the low-redshift sub-DLA listed in Table 3. For the 'object 2', no detections are made in SDSS, but the red colours point to a late-type galaxy at $z \sim 1$, therefore more

Table 4. Summary of the SINFONI detection and upper limits for the new targets from this work.

Quasar	z_{abs}	$F(H\alpha)$ [b] (erg s^{-1} cm^{-2})	Lum(Hα) (erg s^{-1})	SFR (M$_\odot$ yr^{-1})	Id method	References
SDSS J002133.27+004300.9	0.941 87[a]	$1.8 \pm 1.1 \times 10^{-16}$	$8.1 \pm 4.8 \times 10^{41}$	3.6 ± 2.2	Proximity	Rao et al. (2011)
Q0052+0041	0.7402	$<1.6 \times 10^{-17}$	$<0.40 \times 10^{41}$	<0.18	Spectroscopy	Lacy et al. (2003)
SDSS J011615.51−004334.7	0.9127	$<0.7 \times 10^{-17}$	$<0.30 \times 10^{41}$	<0.13	Photo-z	Rao et al. (2011)
J0138−0005	0.7821	$<1.9 \times 10^{-17}$	$<0.55 \times 10^{41}$	<0.24	Proximity	Rao et al. (2011)
J045647.17+040052.9	0.8596	$<1.9 \times 10^{-17}$	$<0.70 \times 10^{41}$	<0.31	Proximity	Le Brun et al. (1997)
Q0826−2230	0.9110	$<0.1 \times 10^{-17}$	$<0.04 \times 10^{41}$	<0.02	Proximity	Meiring et al. (2011)
SDSS J152102.00−000903.1	0.9590	$<2.1 \times 10^{-17}$	$<1.01 \times 10^{41}$	<0.45	Proximity	Rao et al. (2011)

Notes. [a]In the case of SDSS J002133.27+004300.9, z_{abs} is derived from the Hα emission of the absorbing galaxy observed with SINFONI.
[b]The 2.5σ upper limits for non-detections are computed for an unresolved source spread over 32 spatial pixels and spectral FWHM = 6 pixels = 9 Å.

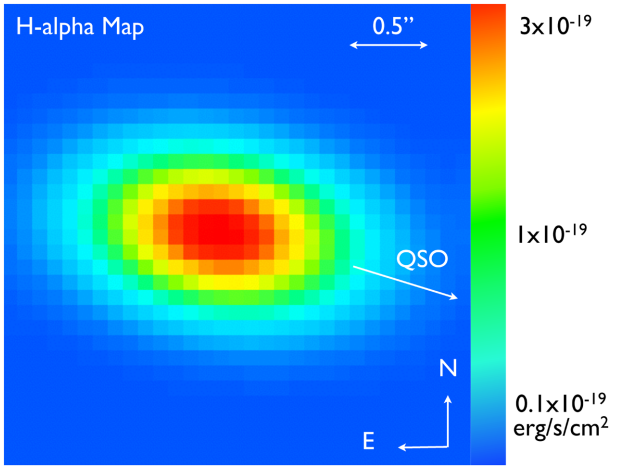

Figure 1. Hα flux map of the sub-DLA–galaxy towards SDSS J002133.27+004300.9 at $z_{abs} = 0.9420$ convolved with the model. The quasar is not covered by our data. The orientation and scales are indicated on the figures as well as the direction to the quasar.

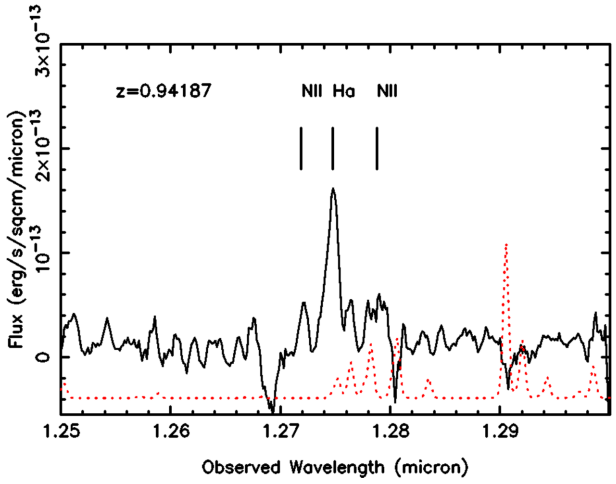

Figure 2. 1D SINFONI Hα line detection of the absorbing galaxy towards SDSS J002133.27+004300.9. The integrated spectrum over 13 pixels circular aperture of the redshifted Hα emission line of the absorbing galaxy. The units are in erg s^{-1} cm^{-2} μm^{-1}. The spectrum is smoothed (5 pixel boxcar). The dotted spectrum at the bottom of the panel is the sky spectrum with arbitrary flux units, scaled for clarity, and indicating the position of the OH sky lines.

likely matching the higher redshift sub-DLA. Indeed, our SINFONI observations confirm that this galaxy's redshift corresponds to the one from the $z_{abs} = 0.9420$ sub-DLA. We report the detection of the Hα emission line at $z = 0.941\,87$. Fig. 1 shows the Hα flux map of this galaxy convolved with the model. We measure an Hα flux of $1.8 \pm 1.1 \times 10^{-16}$ erg s^{-1} cm^{-2}, corresponding to a luminosity $L(H\alpha) = 8.1 \pm 4.8 \times 10^{41}$ erg s^{-1} (see Table 4). We then derive the SFR assuming the Kennicutt (1998) flux conversion corrected to a Chabrier (2003) IMF, leading to SFR = 3.6 ± 2.2 M$_\odot$ yr^{-1} (no dust correction) at an angular separation of 10.8 arcsec (corresponding to an impact parameter of 85 kpc). Fig. 2 shows the 1D integrated spectrum extracted from the SINFONI cube and zoomed around the Hα emission line. While Hα is clearly detected, [N II] is not seen with a flux limit less than 3.97×10^{-16} erg s^{-1} cm^{-2}. Using the N2-parameter (Pettini & Pagel 2004) based on our limit on the [N II] λ6585/Hα ratio, we can derive a limit on the emission metallicity: 12+log(O/H) < 9.10, which is not very constraining in this case.

To estimate the kinematics of the host galaxy, we use the GalPak^{3D} algorithm (Bouché et al. 2015) which compares directly the data cube with a parametric model mapped in x, y, λ coordinates. The algorithm uses a Markov chain Monte Carlo (MCMC) approach with a non-traditional proposed distribution in order to efficiently probe the parameter space. This algorithm is able to recover the morphological parameters (inclination, position angle) to within 10 per cent and the kinematic parameters (maximum rotation velocity) within 20 per cent, irrespective of the seeing (up to 1.2 arcsec) provided that the maximum SNR is greater than ∼3 pixel^{-1} and that the galaxy half-light radius to seeing radius is greater than about 1.5. In our case, the quality of the data for that field is limited due to the fact that only one OB was executed (and classified as 'terminated' by ESO due to degrading seeing to 0.95 arcsec during exposure), resulting with a seeing of 0.75 arcsec. As a result, the SNR in the brightest pixel is about 2.7, i.e. just below the threshold of 3, and a careful look at the MCMC chain is required.

Using a Gaussian flux profile and an arctan velocity profile, we find that its dispersion Σ_o is well constrained at around $\sigma = 123 \pm 11$ km s^{-1}, while the maximum circular velocity is essentially poorly constrained ($V_{max} = 80 \pm 40$ km s^{-1}). The half-light radius has converged to about 6 kpc, and the PA is found to be 60–90 deg, while the inclination and turn-over radius are both unconstrained.

Assuming that the system towards SDSS J002133.27+004300.9 is rotating, we can use the enclosed mass to determine the dynamical mass within $r_{1/2}$ (Epinat et al. 2009):

$$M_{dyn} = V_{max}^2 r_{1/2}/G, \quad (1)$$

where V_{max} and $r_{1/2}$ are measured from the 3D kinematical fit to the SINFONI cube. We therefore find $M_{dyn} = 10^{9.9\pm0.4}$ M$_\odot$.

Table 5. Summary of the X-Shooter detections from the new targets in this work.

Quasar	z_{abs}	Detected?	Flux at Hα position[b] (erg s^{-1} cm^{-2})	Id method	References
SDSS J002133.27+004300.9	0.941 87[a]	Detected	1.76×10^{-16}	Proximity	Rao et al. (2011)
Q0052+0041	0.7402	Bright continuum	2.0×10^{-18}	Spectroscopy	Lacy et al. (2003)
SDSS J011615.51−004334.7	0.9127	Faint continuum	1.2×10^{-18}	Photo-z	Rao et al. (2011)
J045647.17+040052.9	0.8596	Undetected ($b = 0.8$ arcsec)	–	Proximity	Le Brun et al. (1997)
Q0826−2230	0.9110	Undetected	–	Proximity	Meiring et al. (2011)
SDSS J122836.8+101841.7	0.9376	Faint continuum	1.2×10^{-18}	Photo-z	Rao et al. (2011)
SDSS J152102.00−000903.1	0.9590	Very faint continuum	0.5×10^{-18}	Proximity	Rao et al. (2011)

Notes. [a]In the case of SDSS J002133.27+004300.9, z_{abs} is derived from the Hα emission of the absorbing galaxy observed with SINFONI. [b]The values are fluxes in the continuum detected with X-Shooter averaged over a dozen pixels, except for SDSS J002133.27+004300.9 which is the detected flux in the detected emission line. These fluxes are significantly below the SINFONI detection limits (see Table 4).

We are able to estimate the mass of the halo in which the system towards SDSS J002133.27+004300.9 resides, assuming a spherical virialized collapse model (Mo & White 2002):

$$M_{halo} = 0.1 H_o^{-1} G^{-1} \Omega_m^{-0.5} (1+z)^{-1.5} V_{max}^3, \quad (2)$$

using inclination-corrected V_{max} value. We find $M_{halo} = 10^{11.9 \pm 0.5}$ $M_\odot$. This halo mass is comparable with the one from the Milky Way: $1.9^{+3.6}_{-1.7} \times 10^{12}$ $M_\odot$ (Wilkinson & Evans 1999).

3.2 X-Shooter detections

Our X-Shooter observations include several detections of the absorbing galaxies. We detail our findings for each individual object in turn below. Table 5 summarizes the results.

SDSS J002133.27+004300.9: in the section above, we reported detection of Hα at the expected position of the absorbing galaxy in this field. The X-Shooter observations confirm this detection. The Hα line is clearly seen in each 2D frame from individual OBs. The detections are even stronger in the most recent observations (taken in 2015 July) notwithstanding that the requested constraints on the observing conditions are similar. An excerpt 2D frame is shown in the top panel of Fig. 3. The feature is clearly extended along the dispersion axis. The bottom panel of Fig. 3 shows the 1D extracted spectrum together with a sky spectrum (red dotted line). We measure an Hα flux of $F(H\alpha) = 1.76 \times 10^{-16}$ erg s^{-1} cm^{-2}, almost identical to our measurement from SINFONI observations (see Table 4). The agreement between the two measurements is remarkable given the uncertainties in flux calibration inherent to the X-Shooter instrument.

There are strong hints of the presence of the [N II] λ6585.27 emission line too (see Fig. 3). However, we notice the presence of an OH sky line at this wavelength. For this reason, we conservatively report a limit on the [N II] flux of $F([N\,II]) < 1.7 \times 10^{-18}$ erg s^{-1} cm^{-2}. Similarly, we report $< 1.1 \times 10^{-18}$ erg s^{-1} cm^{-2} from the non-detection of the [N II] λ6549.86 in the X-Shooter NIR arm. In the VIS arm, the non-detection of both [O III] and [O II] doublets results in the following flux limits: $F([O\,III]\,\lambda5008) < 0.7 \times 10^{-18}$, $F([O\,III]\,\lambda4960) < 0.7 \times 10^{-18}$, $F([O\,II]\,\lambda7243) < 0.8 \times 10^{-18}$ and $F([O\,II]\,\lambda7237) < 0.8 \times 10^{-18}$ erg s^{-1} cm^{-2}.

Q0052+0041: Lacey et al. (2003) used an *HST* spectrum of this quasar to measure an H I column density of $\log N(H\,I) = 20.4 \pm 0.1$. In addition, Lacey et al. (2003) reported the presence of the absorbing galaxy in this field based on both NIR imaging and a Keck/Low Resolution Imaging Spectrometer spectrum showing [O II] emission and Ca H&K absorption. The authors report that the object is a fairly normal, star-forming galaxy with a luminosity of approximately L_*. The [O II] and Ca H&K lines present a slight velocity offset which is also reflected in the absorption profiles of Mg II, Mg I and Fe II. It is noted that these two components might either correspond to two distinct galaxies, one of which is a dwarf which remains undetected. Alternatively, this shift could be due to motion of internal gas in the main galaxy. Lacey et al. (2003) do not measure the flux in the [O II] line or give an estimate for the SFR, however.

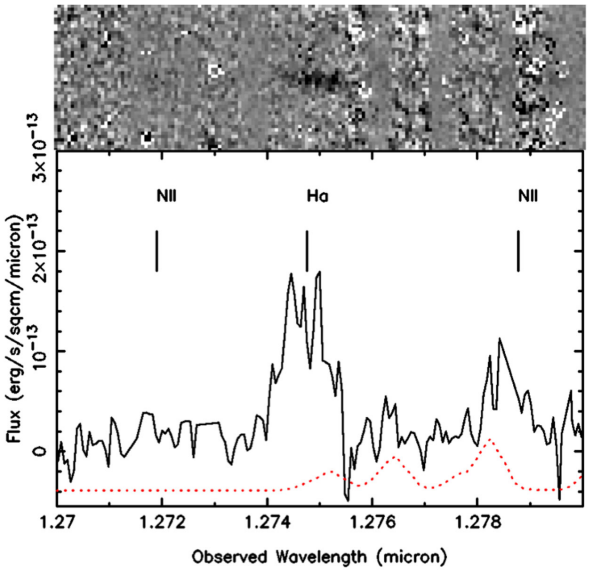

Figure 3. 1D X-Shooter NIR arm revealing the Hα line in the absorbing galaxy towards SDSS J002133.27+004300.9. The units are in erg s^{-1} cm^{-2} μm^{-1}. The spectrum is not smoothed. The dotted spectrum at the bottom of the panel is the sky spectrum with arbitrary flux units, scaled for clarity, and indicating the position of the OH sky lines. The top panel shows the 2D emission line on the same wavelength scale.

Based on the X-Shooter observations, we report the detection of a bright continuum at the expected position of the absorbing galaxy. As in our SINFONI observations, we do not detect Hα in that object in NIR arm of X-Shooter (down to $F(H\alpha) < 1.6 \times 10^{-17}$ erg s^{-1} cm^{-2}). However, we do report [O II] at the expected position of the absorbing galaxy based on the VIS arm of the X-Shooter spectrum. The [O II] doublet is unresolved notwithstanding the X-Shooter spectral resolution. The Ca H&K are not detected, but we note that the SNR of our spectrum is lower than the Keck/Echelle Spectrograph and Imager (ESI) spectrum of Lacy et al. (2003). Fig. 4 shows the 1D extracted spectrum showing a rather broad emission. Based on this detection, we derive $F([O\,II]) = 1.9 \pm 0.3 \times 10^{-17}$ erg s^{-1} cm^{-2}, which translates into a luminosity of

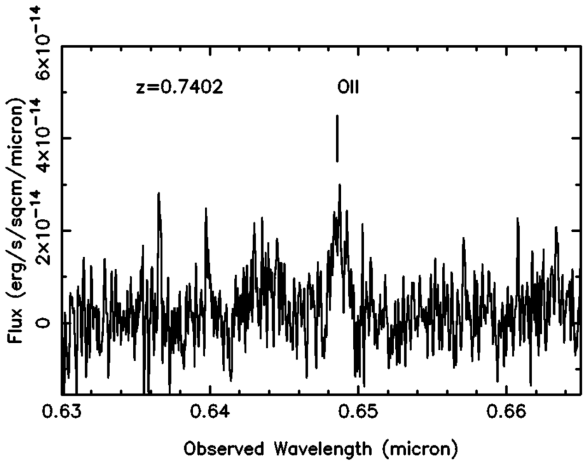

Figure 4. 1D X-Shooter VIS arm revealing [O II] λ3727 line in the absorbing galaxy towards Q0052+0041. The units are in erg s^{-1} cm^{-2} μm^{-1}. The spectrum is smoothed (5 pixel boxcar). From a careful inspection of the individual exposures, we can tell that the other narrower features bluer of [O II] are spurious.

$L([\mathrm{O\,II}]) = 3.8 \pm 0.6 \times 10^{41}$ erg s^{-1}. Using the prescription from Kennicutt (1998):

$$\mathrm{SFR}_{[\mathrm{O\,textscii}]} = 1.4 \times 10^{41} L([\mathrm{O\,II}]), \quad (3)$$

we derive an SFR $= 5.3 \pm 0.7$ $M_\odot$ yr^{-1} uncorrected for dust depletion. This estimate is well above the limit derived with SINFONI based on the non-detection of Hα (SFR < 0.18 $M_\odot$ yr^{-1}). However, we note that Moustakas, Kennicutt & Tremonti (2006) report a large scatter in the SFR/[O II] relation. In fact, the [O II]/Hα ratio we derive from the non-detection of Hα in this system is extreme and falls away from the relation, which might explain the difference in SFR estimates and which leads to questions about the use of the relation.

SDSS J011615.51−004334.7: Rao et al. (2006) report a sub-DLA at $z_{\rm abs} = 0.9127$ along this line of sight. They measure $\log N(\mathrm{H\,I}) = 19.95^{+0.05}_{-0.11}$. In addition, Rao et al. (2011) used *J*, *H* and *K* ground-based images with Sloan colours of the brightest object detected in the field to perform a photometric redshift estimate. The authors note that their estimate is not in agreement with the photometric redshift in the Sloan data base but that it does marginally agree with the absorption redshift.

In the NIR arm of our X-Shooter observation, we report a faint continuum at the expected position of the absorbing-galaxy candidate. The object presents a power-law continuum and an emission line consistent with the redshift of the background quasar ($z_{\rm em} = 1.275$), but this could be due in part to contamination from the nearby quasar although it is 8.1 arcsec away. The flux at the Hα position averaged over a dozen pixels is $F(\mathrm{H}\alpha) < 1.2 \times 10^{-18}$ erg s^{-1} cm^{-2}, consistent with the non-detection in our SINFONI observations.

J045647.17+040052.9: there are two absorbers reported along this line of sight: an Mg II and C IV absorber at $z_{\rm abs} = 1.1536$ (Steidel & Sargent 1992) and a DLA with $\log N(\mathrm{H\,I}) = 20.75 \pm 0.03$ at $z_{\rm abs} = 0.8596$ (Steidel, Pettini & Hamilton 1995). Using ground-based imaging, Steidel et al. (1995) report an absorbing-galaxy candidate at an angular separation of 2.1 arcsec. However, Le Brun et al. (1997) used *HST* images and report a faint galaxy at an angular separation of 0.8 arcsec. Le Brun et al. (1997) argue that the difference in impact parameters is due to their less accurate quasar PSF subtraction than in the ground-based images of Steidel et al. (1995).

We target the object at angular separation of 0.8 arcsec with our X-Shooter observations but do not report any detections. We note that the small angular separation ($b = 0.8$ arcsec) might have hampered detection in this case. On top of that, the quasar is significantly brighter than in the other fields (V mag $= 16.5$), which might limit our capability to detect an object several orders of magnitude fainter. In fact, we find a weak detection at the expected position of Hα line but the Hα flux is less than a per cent of quasar flux, so we do not claim a detection. We note that Takamiya et al. (2012) put a 3σ upper limit from non-detection of the [O II] emission line flux for the $z = 0.8596$ DLA of $F([\mathrm{O\,II}]) < 8.3 \times 10^{-19}$ erg s^{-1} cm^{-2} assuming a line width of 100 km s^{-1}. They also report an emission line galaxy at $z = 0.0715$ with multiple emission lines and a new Mg II absorber at $z = 1.245$.

Q0826-2230: the sub-DLA at $z_{\rm abs} = 0.9110$ has its $N(\mathrm{H\,I})$ measured by Rao et al. (2006) to be $\log N(\mathrm{H\,I}) = 19.04 \pm 0.04$. Meiring et al. (2011) used Sloan and Southern Astrophysical Research Telescope imaging to obtain photometric redshifts of the absorbing-galaxy candidates in the field. The images show that the quasar is lensed. The closest object, 'object 1', is identified as a star. The next two closest galaxies ('objects 4 and 5') have photometric redshifts which are not consistent with the redshift of the absorber. In our X-Shooter observations, we target 'object 4'. In this case too, we do not report any detections in our X-Shooter observations. Again, as in the case of J045647.17+040052.9, we note that the quasar is significantly brighter than in the other fields (V mag $= 16.2$) creating a high contrast. Recently, Straka et al. (submitted) determine spectroscopically that 'objects 4 and 5' are indeed *not* at the redshift of the absorber.

SDSS J122836.8+101841.7: Rao et al. (2006) report a sub-DLA at $z_{\rm abs} = 0.9376$ along this line of sight. They measure $\log N(\mathrm{H\,I}) = 19.41^{+0.12}_{-0.18}$. In addition, Rao et al. (2011) observed *J*, *H* and *K* ground-based images. They detect two objects in the field and find the photometric redshift of the closer candidate to be consistent with the absorber.

In the NIR arm of our X-Shooter observation, we report a faint continuum at the expected position of the absorbing-galaxy candidate. While this continuum is clearly visible in the 2D images, a careful visual inspection does not show predominant emission lines, rendering its identification and redshift determination difficult. To compare with SINFONI observations, we measure the flux averaged over a dozen pixels in the continuum at the expected position of the Hα emission line ($F(\mathrm{H}\alpha) < 1.2 \times 10^{-18}$ erg s^{-1} cm^{-2}). This flux is significantly below the SINFONI detection limit (see Table 4). In case this object were an early type and bulge-dominated galaxy, we would not expect to detect its Hα emission, but only its continuum. This hypothesis could be checked with further imaging or deeper spectroscopy. Indeed, Rahmani et al. (in preparation) report two such examples where the redshift of the absorbing galaxy is confirmed from absorption lines in the galaxy spectra.

SDSS J152102.00-000903.1: Rao et al. (2006) report a sub-DLA at $z_{\rm abs} = 0.9590$ along this line of sight. They measure $\log N(\mathrm{H\,I}) = 19.40^{+0.08}_{-0.14}$. In addition, Rao et al. (2011) observed *J*, *H* and *K* ground-based images. They detect two objects in the field, but could not derive photometric redshifts for either. They note that the object closer to the quasar has colours consistent with being an early-type galaxy at the absorption redshift and so we targeted that object with our X-Shooter observations.

In the NIR arm, we report a very faint continuum at the expected position of the absorbing-galaxy candidate. The flux at the Hα position averaged over a dozen pixels is

$F(\mathrm{H}\alpha) < 0.5 \times 10^{-18}$ erg s^{-1} cm^{-2}, consistent with the non-detection in our SINFONI observations.

3.3 Quasar absorption spectroscopy

In our sample, just one X-Shooter target (SDSS J002133.27+004300.9) did not include the quasar in the slit due to its large impact parameter. However, this quasar spectrum was observed under programme ESO 078.A-0003 with UVES and the relevant data are part of the Advanced Data Products ESO archive. We use the UVES spectrum observed in Service Mode on 2006 November 16. The object was observed using a combined 390+564 nm setting with exposure time lasting 3000 s. The reduced data are taken from the Phase 3 ESO archive facility (Retzlaff et al. 2014). The resulting spectra are corrected to the vacuum heliocentric reference and then combined by weighting each spectrum by SNR. In order to perform the analysis of the absorption lines associated with the galaxy, the quasar spectrum is normalized using a spline function going through regions devoid of absorption features.

Voigt profile fits are commonly used to derive the column density of different elements detected in absorption in quasar spectra. In this case, Dessauges-Zavadsky, Ellison & Murphy (2009) derive an abundance for iron and an upper limit for zinc: [Fe/H] $= -0.21 \pm 0.14$ and [Zn/H] < -0.41 although no details on the fits are provided. In fact, the UVES quasar spectrum of SDSS J002133.27+004300.9 covers Fe II λλ2600, 2586, 2382, 2260, Zn II λλ2062, 2026, Cr II λλ2056, 2026, Mg II λλ2796, 2803, Mn II λ2576, Mg I λλ2852, 2026, Al III λλ1862, 1854, Si II λ1808 and Ti II λ3384. Here, we perform a fit of the detected transitions using a Voigt profile fit under the MIDAS/FITLYMAN software. The redshift used is set to be the emission systemic redshift of the detected galaxy, $z_{\rm abs} = 0.941\,87$ from the SINFONI observations described above. The different ions share a common absorption profile, and a similar component structure (Doppler parameter and redshift) has been assumed to exist for all species and used throughout the fit. Due to either weak or saturated absorption in most of the covered ions, the components assumed for the fit are chosen based on Fe II lines for the strongest components and Mg II for the weakest components.

A nine-component fit is used, with two isolated blue components at ~ -180 km s^{-1}, and two strong components either side of the absorbing-galaxy systemic redshift. The estimate of the Fe II total column density is consistent with the value reported by Dessauges-Zavadsky et al. (2009) within the errors. The lines of Zn II, Cr II and Mg I are fitted together to deal with the blend around $\lambda_{\rm rest} = 2026$ Å. We use a two-step approach: the two isolated blue components are fitted separately due to limitations in the number of free parameters in the fitting algorithm. Our fit in the Zn II and Cr II region is hampered by the low SNR of the spectrum, so that we only report upper limits: log N(Zn II) < 12.66, resulting in [Zn/H] $< +0.57$ and log N(Cr II) < 12.93, resulting in [Cr/H] < -0.09. The [Zn/H] value is much less constraining than the one reported by Dessauges-Zavadsky et al. (2009) on the same data set. In fact, we calculate that given the column density of Zn II, an SNR $\sim$ 100 would be required to reach the limit reported by Dessauges-Zavadsky et al. (2009). We therefore use our [Zn/H] estimate in the following analysis. Finally, Al III, Mn II and Si II are fitted using the nine components simultaneously. We note that Ti II is covered but undetected and derive an upper limit. The doublet of Mg II is detected but strongly saturated, so only the weaker components are fitted.

The parameters for the profile fits are provided in Table 6 and fits are shown in Fig. 5. The horizontal arrow on the top-left panel

Table 6. Voigt profile fit parameters to the low- and intermediate-ionization species for the $z = 0.941\,87$ log N(H I) $= 19.38^{+0.10}_{-0.15}$ absorber towards SDSS J002133.27+004300.9.

Comp.	$z_{\rm abs}$	b (km s^{-1})	Ion	log N (cm^{-2})
1	0.940 72	8.2 ± 0.4	Fe II	12.47 ± 0.07
			Zn II	–
			Cr II	11.82 ± 1.13
			Si II	–
			Mg I	10.53 ± 0.52
			Al III	12.21 ± 0.14
			Mn II	–
			Mg II	13.09 ± 0.02
2	0.940 87	5.6 ± 0.5	Fe II	11.80 ± 0.013
			Zn II	12.26 ± 0.06
			Cr II	–
			Si II	–
			Mg I	–
			Al III	11.53 ± 0.55
			Mn II	–
			Mg II	12.66 ± 0.02
3	0.941 65	9.0 ± 0.2	Fe II	14.08 ± 0.03
			Zn II	–
			Cr II	12.42 ± 0.18
			Si II	14.99 ± 0.11
			Mg I	12.27 ± 0.01
			Al III	13.88 ± 0.08
			Mn II	11.92 ± 0.16
			Mg II	–
4	0.941 83	2.8 ± 1.0	Fe II	12.53 ± 0.05
			Zn II	11.67 ± 0.11
			Cr II	–
			Si II	–
			Mg I	–
			Al III	12.17 ± 0.15
			Mn II	–
			Mg II	–
5	0.941 92	2.5 ± 0.5	Fe II	12.83 ± 0.07
			Zn II	11.88 ± 0.07
			Cr II	12.18 ± 0.25
			Si II	–
			Mg I	10.80 ± 0.15
			Al III	11.97 ± 0.23
			Mn II	–
			Mg II	–
6	0.942 00	2.1 ± 0.3	Fe II	12.94 ± 0.08
			Zn II	12.16 ± 0.06
			Cr II	11.78 ± 0.61
			Si II	–
			Mg I	10.18 ± 0.64
			Al III	11.47 ± 0.56
			Mn II	–
			Mg II	–
7	0.942 08	1.9 ± 0.6	Fe II	12.69 ± 0.11
			Zn II	10.59 ± 1.16
			Cr II	12.07 ± 0.33
			Si II	13.64 ± 1.16
			Mg I	10.68 ± 0.19
			Al III	12.12 ± 0.22
			Mn II	–
			Mg II	–
8	0.942 14	2.7 ± 1.9	Fe II	12.39 ± 0.10
			Zn II	–
			Cr II	–
			Si II	13.80 ± 0.83
			Mg I	11.11 ± 0.09

Table 6 – *continued.*

Comp.	z_{abs}	b (km s^{-1})	Ion	log N (cm^{-2})
			Al III	12.08 ± 0.20
			Mn II	–
			Mg II	–
9	0.942 33	13.9 ± 0.3	Fe II	14.41 ± 0.04
			Zn II	–
			Cr II	12.30 ± 0.31
			Si II	14.98 ± 0.11
			Mg I	12.80 ± 0.01
			Al III	13.62 ± 0.04
			Mn II	12.20 ± 0.10
			Mg II	–

indicates the maximum velocity measured from SINFONI kinematics study, $V_{max} = 80 \pm 40$ km s^{-1}. It is interesting to note that the weakest blue components at ∼180 km s^{-1} are not explained by the rotation velocity of the disc in that object. In addition, we apply the method proposed by Jenkins (2009) to both the strong red group of components and to the blue group of components following the method described by Quiret et al. (submitted). In short, this method determines a combination of metallicity (from metal and H I column densities) and dust content using the Milky Way sightlines as references for the depletion pattern. Here, we used it to derive the metallicity of group of components for which we do not have a direct measure of N(H I) due to blending. We find that the metallicity is higher in the red group of components (N(H I)+[X/H] = 19.5) at the position of the systemic redshift of the absorbing galaxy than in the blue group of components (N(H I)+[X/H] = 17.6), consistent with a picture where this latter gas is associated with metal-poor accreting gas (Bouché et al. 2013).

The total column densities and abundances are with respect to solar values using the convention [X/H] = log (X/H)−log (X/H)$_\odot$ and are listed in Table 7. Most notably, we derive [Fe/H] = −0.27 ± 0.18, [Si/H] = +0.42 ± 0.23 and [Cr/H] < −0.09. Our findings indicate that the metallicity of the system is above solar, [Si/H] = +0.42 ± 0.23, which is common amongst low-redshift, low-N(H I) quasar absorbers (Som et al. 2015; Quiret et al., submitted). We note

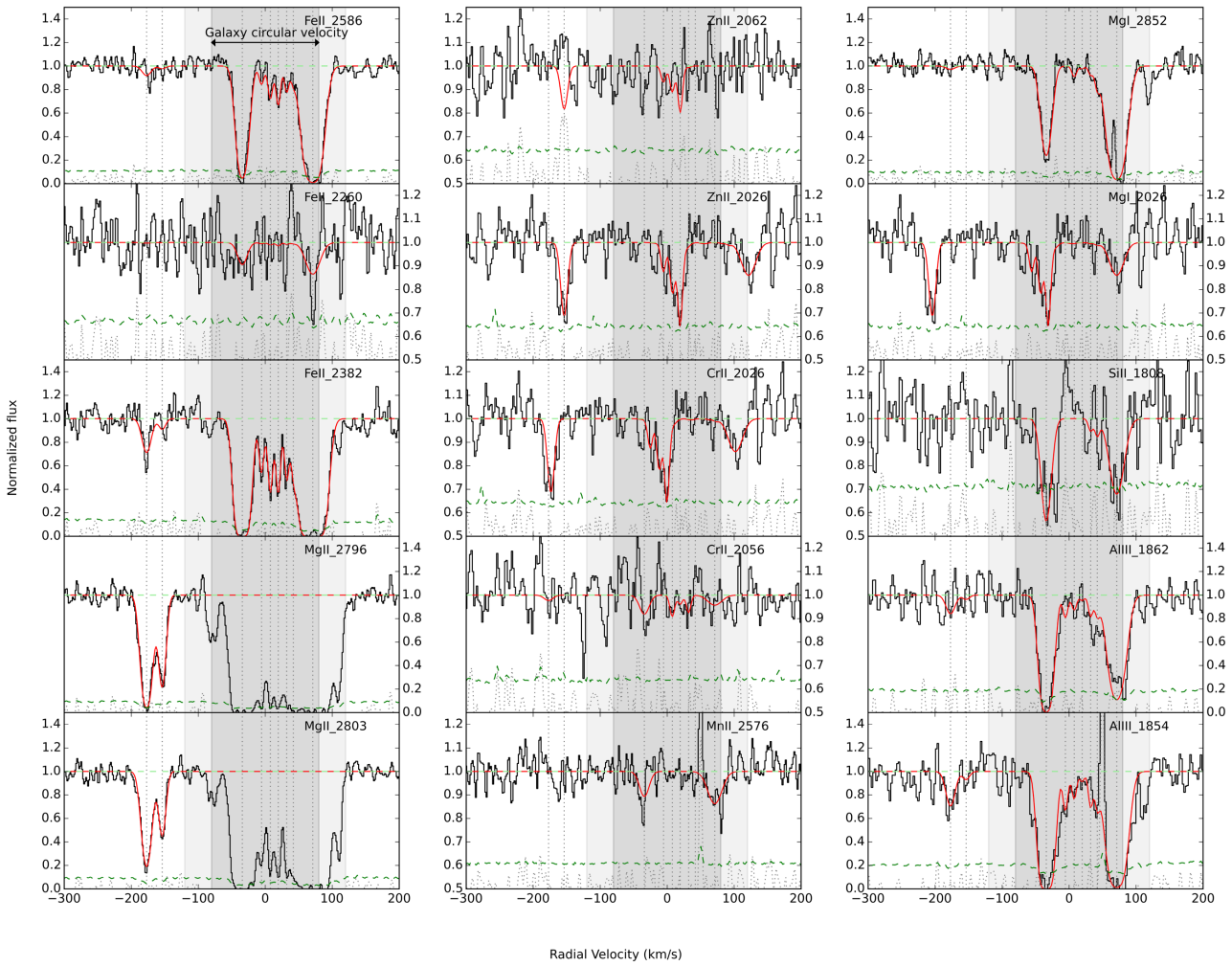

Figure 5. Normalized 1D UVES quasar spectrum of SDSS J002133.27+004300.9. The normalized UVES spectrum (black) and the Voigt profile fits (red) of the sub-DLA are shown on a velocity scale where 0 km s^{-1} is set to be the emission systemic redshift of the detected galaxy, $z_{abs} = 0.941\,87$. The positions of the components are indicated by vertical dotted lines. The error array is shown as a dashed green line and the difference between the UVES spectrum and the fit is shown as a dotted light grey line. For weaker lines, the y-axis scale is adjusted and these latter (error + difference) spectra are shifted up by 0.5. The horizontal arrow on the top-left panel and the dark and light grey bands in all panels indicate the maximum velocity measured from SINFONI kinematics study, $V_{max} = 80 \pm 40$ km s^{-1}. The weakest blue components at ∼180 km s^{-1} are not explained by the rotation velocity of the disc in that object.

Table 7. Neutral gas-phase abundances of SDSS J002133.27+004300.9 from UVES quasar spectroscopy. These metallicities with respect to solar values are measured in absorption along the line of sight to the background quasar.

Element	Column density of II ions	Abundance
Fe	14.61 ± 0.03	-0.27 ± 0.18
Zn	<12.66	$<+0.57$
Cr	<12.93	<-0.09
Si	15.31 ± 0.08	$+0.42 \pm 0.23$
Mg	13.23 ± 0.02	-1.75 ± 0.17
Mn	12.38 ± 0.09	-0.43 ± 0.24
Al	14.10 ± 0.05	$+0.27 \pm 0.20$
Ti	<12.02	<-0.31

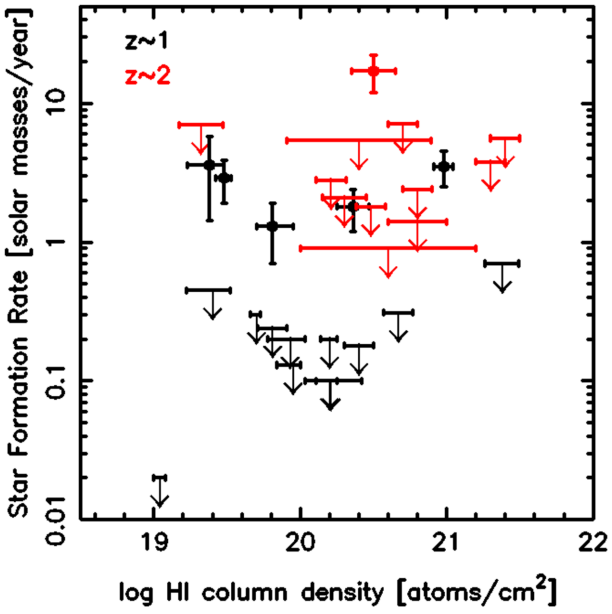

Figure 6. SFR estimates for the full N(H I)-selected SINFONI survey. The black crosses refer to $z \sim 1$ targets observed in the J band with SINFONI, while the red crosses are objects lying at $z \sim 2$ observed in the K band.

that in this system, [Al/Fe] is above solar in many components due to anomalously strong Al II features. It is not clear whether this is due to photoionization effects, differential depletion, hidden saturation or nucleosynthetic yields differing from the standard picture of uniform yields from Type II SNe and and Type I SNe at a given redshift.

The remaining targets do not have high-resolution ($R \sim 40\,000$) quasar spectra available. They are however all covered by our X-Shooter observations. In a subsequent work, we will derive detailed abundance estimates for these low-redshift DLAs and sub-DLAs.

4 RESULTS

4.1 Global properties of the SINFONI survey

Fig. 6 summarizes the SFR estimates and limits as a function of N(H I) for the full N(H I)-selected SINFONI survey (Péroux et al. 2011a, 2012, and this work). The targets are selected so that they have their N(H I) measured from *HST* spectroscopy. The black crosses refer to $z \sim 1$ targets observed in the J band with SINFONI, while the red crosses are objects lying at $z \sim 2$ observed in the K band. Taken together, the detection rates of the N(H I)-selected SINFONI survey are 33 per cent (6/18) at $z \sim 1$ and 8 per cent (1/12) at $z \sim 2$, although number statistics remain small. Interestingly, Fumagalli et al. (2010) used a different technique at $z > 2$ to search for absorbing galaxies and report a significantly lower detection rate. These authors target quasar sightlines with multiple optically thick H I absorbers and use the higher redshift system as a 'blocking filter' (via its Lyman-limit absorption) to eliminate all far-ultraviolet (FUV) emission from the quasar. This allows them to directly image the rest-frame FUV continuum emission of the lower redshift DLA, without any quasar contamination. The difference in detection rates with respect to our survey might arise from the fact that these authors measure SFR at FUV wavelengths which is prone to strong dust extinction effects although the authors have inferred minimal dust depletion from abundance studies in their sample. In our SINFONI survey, we are observing at NIR wavelengths (visible wavelengths in the absorber rest frame) thus minimizing the effect from dust obscuration.

Even with these rather low detection rates, one might rightly raise the question whether the galaxy identified at the redshift of the absorber is directly associated with it. To answer this question, we used the *REF L050N512* simulation from the OWLS project (Schaye et al. 2010) to look at the properties of galaxies associated with absorbers. We note that this cosmological simulation successfully reproduces both the cosmic SFR (Schaye et al. 2010) and H I column density distribution function (Rahmati et al. 2013) at $z = 1$. Following the approach presented in Rahmati & Schaye (2014), we searched for absorbers with $N(\mathrm{H\,I}) > 10^{19}$ cm^{-2} that have a galaxy with SFR>1 M$_\odot$ yr^{-1} within a search (projected) radius of 40 kpc corresponding to our early blind search survey (Péroux et al. 2012, 2013). We found that only < 10 per cent of the selected absorbers have fainter companion galaxies (with $0.01 <$ SFR < 1 M$_\odot$ yr^{-1}) within the same search radius and at most 40 per cent within 100 kpc (corresponding to the targeted detection reported here). While this fraction rises strongly with increasing radius and redshift, our calculation is consistent with the idea that galaxies identified in our survey are directly associated with the DLAs and sub-DLAs.

Fig. 6 also shows that the SFR limits derived from non-detections are more stringent at $z \sim 1$ than at $z \sim 2$ and that the object detected at $z \sim 2$ (towards Q2222−0946) has a high SFR. In addition, we target higher N(H I) systems at high redshift than at $z \sim 1$. In the sample presented here, it is interesting to point out that the non-detections of the absorbing galaxies arise from a mixed bag of candidates based on both broad-band imaging and proximity to the quasar and/or photometric redshifts based on colours. Conversely, the SINFONI+X-Shooter detection towards SDSS J002133.27+004300.9 is based on an absorbing-galaxy candidate with no a priori spectroscopic or photometric redshift.

Fig. 7 illustrates various properties of the absorbing galaxies detected in the SINFONI survey as a function of impact parameter. Again, the black points are for systems at $z \sim 1$ and the red ones for the system at $z \sim 2$. We note that the new detection reported here has a larger impact parameter ($b = 86$ kpc) than previously reported objects, although no galaxies are seen at smaller impact parameters in this field (Rao et al. 2011). The left-hand panel of Fig. 7 shows the SFR estimates which do not indicate a trend with impact parameter. The middle panel of Fig. 7 illustrates the evolution of the H I column density N(H I) as a function of impact parameter. As expected, a correlation between these two quantities is observed in our data. This can be naturally understood in a context where these high-redshift quasar absorbers are the analogues of the H I-rich local discs which are known to have H I profiles declining with radius or where we

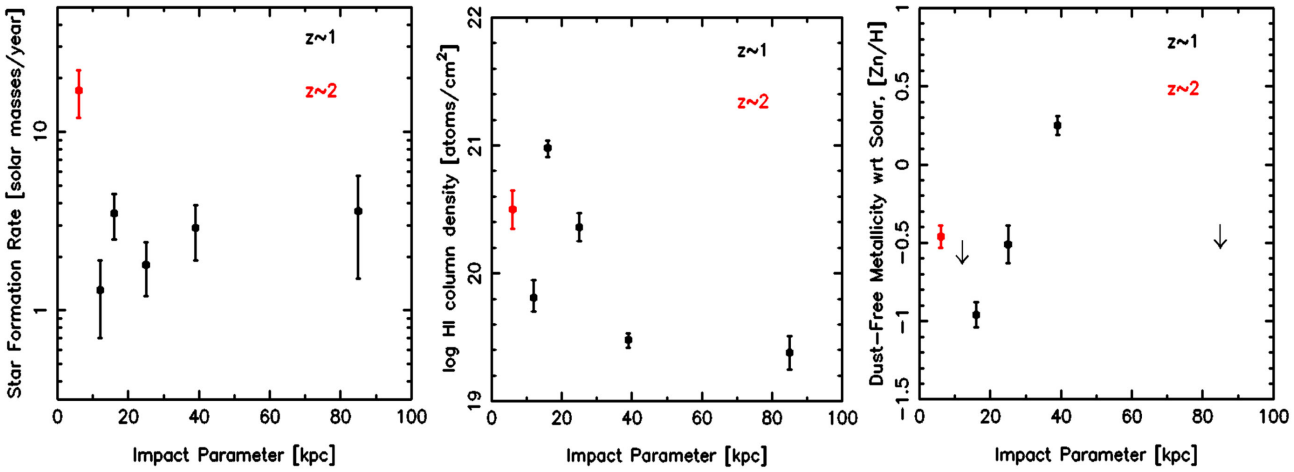

Figure 7. Properties of the absorbing galaxies detected in the SINFONI survey as a function of impact parameter. The black points are for systems at $z \sim 1$ and the red one for the system at $z \sim 2$. We note that the new detection reported here has a larger impact parameter ($b = 86$ kpc) than previously reported objects.

Table 8. Azimuthal angle and metallicity difference. In our SINFONI survey, the neutral gas metallicity with respect to solar values is measured in absorption along the line of sight to the background quasar. The neutral gas abundances listed is based on the undepleted Zn unless stated otherwise. We note that our target selection requiring systems with known N(H I) is key to abundance measurements in absorption. In addition, the SINFONI and X-Shooter detections of the absorbing galaxies provide a measure of the integrated metallicity in the H II regions probed in emission. The metallicity difference between the galaxy and the absorbing gas is the underabundance in neutral phase as defined by Lebouteiller et al. (2013): $\delta_{\rm H\,I}(X) = \log(X/{\rm H})_{\rm H\,II} - \log(X/{\rm H})_{\rm H\,I}$.

Quasar	Azi. angle (deg)	$\log(X/{\rm H})_{\rm H\,II}$	$\log(X/{\rm H})_{\rm H\,I}$	$\delta_{\rm H\,I}(X)$	$M_{\rm halo}$ ($M_\odot$)	References
J002133.27+004300.9	10	$<+0.44$	$<+0.57$	<-0.13	$10^{11.9}$	This work
Q0302−223	70	$+0.04 \pm 0.20$	-0.51 ± 0.12	$+0.55 \pm 0.23$	–	Péroux et al. (2011a)
Q0452−1640	26	-0.46 ± 0.20	-0.96 ± 0.08	$+0.50 \pm 0.21$	$10^{12.8}$	Péroux et al. (2012)
Q1009−0026	50	$+0.04 \pm 0.80$	$+0.25 \pm 0.06$	-0.21 ± 0.80	$10^{12.6}$	Péroux et al. (2011a)
J1422−0001	15	-1.3 ± 0.3	-0.1 ± 0.4	-1.2 ± 0.5	$10^{11.3}$	Bouché et al. (submitted)
J165931+373528	87	-0.21 ± 0.08	-1.12 ± 0.02^a	$+0.91 \pm 0.08$	–	Kacprzak et al. (2014)
Q2222−0946	45	<-0.46	-0.46 ± 0.07	$<+0.0$	–	Péroux et al. (2012)
HE2243−60	20	-0.32 ± 0.10	-0.72 ± 0.05	$+0.40 \pm 0.11$	$10^{11.6}$	Bouché et al. (2013)
Q2352−0028	27	-0.26 ± 0.03	<-0.51	$>+0.25$	$10^{11.8}$	Péroux et al. (2012)

Notes. [a][X/H] based on Mg I, Mg II, Si II, Si III and CLOUDY modelling (Kacprzak et al. 2014).

are probing gradients in the matter density around galaxies at larger radius. Indeed, the background density close to galaxies is higher than far from them, so that larger N(H I) quasar absorbers are present closer to overdensity peaks where massive galaxies are forming (Rahmati & Schaye 2014). The right-hand panel of Fig. 7 presents neutral gas H I metallicity from the weakly depleted element Zn II (Pettini et al. 1994) as a function of impact parameter. We do not see indications of decreasing metallicity with increasing distance from the centre of the galaxy. This is surprising given that metallicity gradients are known to occur in various types of galaxies (Queyrel et al. 2012; Swinbank et al. 2012) and can be seen as further evidence that the gas probed in absorption might be tracing gas flows outside the galaxy's halo. We note that these measurements correspond to the absolute metallicity of the absorbing gas, independent of the emission line metallicity of the associated galaxy.

4.2 Gas flow probes

Recent studies (Bordoloi et al. 2011; Bouché et al. 2012, 2013; Schroetter et al. 2015) argue that absorption aligned with the minor axis of a galaxy can be modelled by bipolar winds. Thanks to our SINFONI observations, we are able to determine the absorbing-galaxy inclination derived from the ratio of apparent major to minor axis. In addition, we can determine the alignment between the quasar sightline and the projection on the sky of the galaxy's axes. Indeed, Integral Field Unit (IFU) spectroscopy is crucial to untangle the geometric effects related to the location of the quasar sightline. It has been shown in the past by several authors (e.g. Bouché et al. 2012) that a bimodal distribution of the azimuthal orientation of the quasar sightlines with respect to the galaxy major axis allows one to distinguish winds from gas associated with the disc. In this picture, the outflowing gas preferentially leaves the galaxy along its minor axis (path of least resistance) and inflowing gas is almost co-planar with the galaxy disc (i.e. seen preferentially along the major axis; Shen et al. 2012). The azimuthal angle between the quasar line of sight and the projected galaxy's major axis on the sky for objects detected in our SINFONI survey and from the literature are listed in Table 8.

Besides these geometry aspects, a key diagnostic to untangle infalling from outflowing gas around galaxies is the metallicity of the gas. Indeed, metals are known to be produced by stars within galaxies, which will then further enrich the outflowing gas. Conversely, infalling gas feeding galaxies from the filaments of the cosmic web is expected to be pristine. Using these lines of argument, Lehner et al. (2013) and Wotta et al. (in preparation) report a bimodality in the metallicity distribution of Lyman-limit systems (LLS) at

$z < 1$. These authors interpret this result as a signature of some LLS probing infalling gas while other LLS would be related to the absorbing galaxy or associated outflowing gas. A similar behaviour is reported by Quiret et al. (submitted) for sub-DLAs with $z < 1.25$. We note however that these measurements do not provide information about the metallicity of the absorbing galaxy.

In our SINFONI survey, the neutral gas metallicity with respect to solar values is measured in absorption along the line of sight to the background quasar. A summary of these measurements is included in Table 8. The neutral gas abundance is derived from the undepleted Zn abundance in all cases. We note that our target selection including systems with known $N(\mathrm{H\,I})$ is key to abundance measurements in absorption. In addition, the SINFONI and X-Shooter detections of the absorbing galaxies provide a measure of the integrated metallicity in the H II regions probed in emission. The error estimates in these metallicity differences are based on the errors in the emission and absorption metallicities added in quadrature. Again, these values are listed in Table 8 with respect to solar.

Given this information, we are able to compute the metallicity difference between the stars in the galaxy and the absorbing gas in the SINFONI sample. We use the underabundance in neutral phase as defined by Lebouteiller et al. (2013):

$$\delta_{\mathrm{H\,I}}(X) = \log(X/\mathrm{H})_{\mathrm{H\,II}} - \log(X/\mathrm{H})_{\mathrm{H\,I}}. \quad (4)$$

These values provide an estimate of the relative metallicity of the gas probed in absorption with respect to the metallicity in the absorbing galaxy itself. Here, we use neutral gas abundances based on the element Zn, which is only weakly depleted on to dust grains (Pettini et al. 1994). A positive $\delta_{\mathrm{H\,I}}(X)$ value indicates a neutral gas metallicity lower than the galaxy's H II regions, a possible indicator of gas inflow. Conversely, a null or negative $\delta_{\mathrm{H\,I}}(X)$ value indicates an equal or higher metallicity in the absorbing gas than in the galaxy, possibly indicating outflowing gas enriched by star formation within the galaxy.

In Fig. 8, we plot the metallicity difference as a function of azimuthal angle, two independent indicators of gas flows. In this plot, we expect infalling gas to lie in the upper-left corner (low azimuthal angle and high $\delta_{\mathrm{H\,I}}(X)$ value), while outflowing gas would lie in the lower-right corner (high azimuthal angle and low $\delta_{\mathrm{H\,I}}(X)$ value). These are indicated as red arrows in the figure. In addition, we plot the eight objects from our SINFONI survey as well as one object from the literature (Kacprzak et al. 2014) for which all these measurements are available. We note that the few observations available so far do not correlate as expected from simple assumptions. Indeed, the galaxy to gas metallicity difference appears positive in systems with high azimuthal angles while low azimuthal angles cover various metallicity differences including negative values. Quantitatively, we derive a correlation coefficient of 0.30 indicating a weak anticorrelation and a probability $P = 0.43$ of no correlation. In particular, we report no system which would be equally or more metal rich in the distant absorbing gas than in the emission line gas in the galaxy and aligned with the minor axis of the disc as expected from outflows (i.e. bottom-right corner of Fig. 8).

4.3 Discussion

While we chose to present here neutral gas-phase abundances derived from Zn, we note that using Fe provides both a similar number of measurements and a similar trend, only shifted upwards in metallicity values and with additional complications due to dust depletion. Since only a few Si measurements are available for the systems in this sample, and Si is anyway depleted on to dust grains, no robust

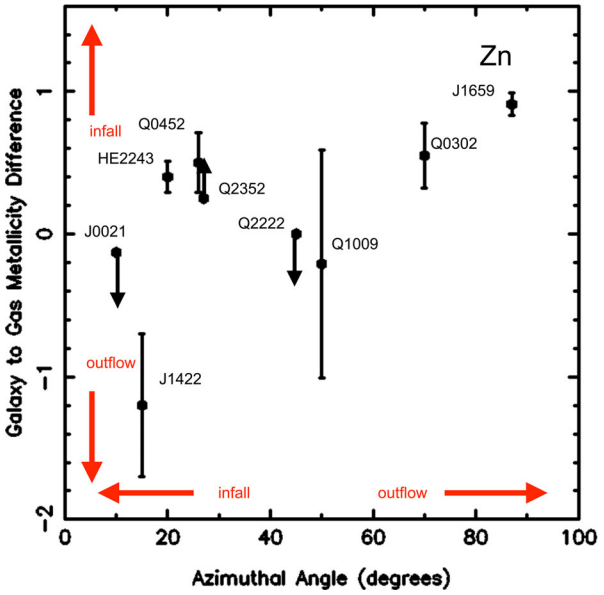

Figure 8. Metallicity difference as a function of azimuthal angle. In this plot, we expect (van de Voort & Schaye 2012) infalling gas to lie in the upper-left corner (low azimuthal angle and high $\delta_{\mathrm{H\,I}}(X)$ value), while outflowing gas would lie in the lower-right corner (high azimuthal angle and zero or negative $\delta_{\mathrm{H\,I}}(X)$ value). These are indicated as red arrows in the figure. Additional observations are necessary to better relate metallicity and geometry in gas flows.

conclusions can be derived based on this element. It is important to note that the metallicity estimates measured in the galaxy and in its outskirts are based on different phases of gas: the emission metallicity traces the ionized gas, while the absorption metallicity traces the neutral phase of the gas. In addition, the emission metallicities reported here use a number of different indicators ranging from R_{23} (Pagel et al. 1979) to the [N II]/Hα parameter (Pérez-Montero & Contini 2009). For example, five systems in our sample (namely J002133.27+004300.9, Q1009−0026, J1422−0001, J165931+373528 and Q2222−0946) have their H II metallicity derived from [N II]/Hα, including two (J002133.27+004300.9 and Q2222−0946) for which [N II] was not detected giving rise to an upper limit in metallicity. The uncertainties in the measurements for the remaining three systems are evidenced by fairly large error bars. The other objects have more reliable H II metallicity measured from R_{23} based on multi-emission line detections in X-Shooter observations (Péroux et al. 2011a, 2012; Bouché et al. 2013).

Similarly, the robustness of the measurements of the azimuthal angle in these systems varies from one object to another. For example, the kinematic properties of the system presented here, J002133.27+004300.9, are rather poorly constrained as described in previous sections. Another example of this is Q2222−0946, which is a compact galaxy with a small impact parameter to the quasar's line of sight ($b = 6$ kpc). Péroux et al. (2012) derive an azimuthal angle of 45 deg which on its own cannot be used to disentangle inflows from galactic winds based on geometric arguments.

Finally, we note that the system reported here, J002133.27+004300.9, has a large impact parameter ($b = 85$ kpc) which might be uncommon for DLA–galaxy association (Rahmani et al., in preparation), but typical of CGM regions (Shull 2014). On the other hand, some other systems have significantly smaller impact parameters (namely Q2222−0946 again) which questions whether the gas probed in absorption is related to CGM regions or more likely to internal parts of the galaxy.

Keeping these limitations in mind, it is interesting to explore the interpretation of this rather unexpected result. Clearly, Fig. 8 suggests that the phenomenon of gas flows may be more complicated and metallicity and geometry might be rather indirect tracers of gas flows (Bouché et al. 2007; Lehner et al. 2013). For example, not all of the gas detected in absorption might be related to the CGM of the galaxy. Indeed, some of it could be related to the rotating gas in the disc of the galaxy itself (Bouché et al. 2013). In fact, a comparison of the $V_{\rm max}$ values when available and the total absorption width might bring some quantitative information on this effect, but we note that in most cases it will bring the data points to higher $\delta_{\rm H\,I}(X)$ values (because $V_{\rm max}$ represent just a fraction of the total absorption profile in most cases), whether they lie at small or large azimuthal angles. Specifically, the $V_{\rm max}$ in the case of Q2222−0946 and J165931+373528 is unknown because the object is compact in the former case and no IFU data are available in the latter case. Interestingly, the whole of the absorption profile along Q1009−0026 matches quite well the $V_{\rm max}$ in that system, so that this data point is not expected to move towards more positive $\delta_{\rm H\,I}(X)$ values. In the case of J1422−0001, Bouché et al. (submitted) report that the inflowing material is considerably metal rich hinting towards recycling material, hence its position in the lower-left corner of the diagram. For the remaining systems, $V_{\rm max}$ is smaller than the actual spread of the absorption profile, and as such would all have slightly more positive $\delta_{\rm H\,I}(X)$ values. Also, Fig. 8 suggests that some systems (in the upper-right corner) may consist of outflows of metal-poor gas, possibly hinting to gas gets ejected before undergoing much star formation.

In addition, simulations indicate that inflows and outflows are complex phenomena. Hot accretion inflows are not expected to align along any preferred direction (Ocvirk, Pichon & Teyssier 2008; Nelson et al. 2015). Indeed, some of our galaxies have high halo masses (see Table 8), and may be cases of hot mode accretion. Gas flows can potentially be affected by numerous shocks (Keres et al. 2005). Similarly, some of the gas is likely to be multi-phase and clumpy, therefore limiting the extent to which a given absorption region represents the halo, given that it comes from only one quasar on a random sightline. Moreover, some of the gas expelled by outflows might not escape the potential well of the galaxy, falling back as galactic fountains but already polluted by metals from star formation (Dekel & Silk 1986; Efstathiou 2000; Cresci et al. 2015). Such systems will be as metal rich in absorption as the galaxy (lower part of Fig. 8) and potentially still be co-planar to the disc (left part of Fig. 8). Such processes might therefore explain the objects populating the bottom-left corner of the figure. An example of this is the absorbing system towards J1422−0001. Overall, additional observations are necessary to better relate metallicity and geometry in gas flows. With the new Multi Unit Spectroscopic Explorer instrument on VLT (Contini et al. submitted) and on longer term the High Angular Resolution Monolithic Optical and Near-infrared Integral field spectrograph IFU on the European-Extremely Large Telescope (Evans et al. 2015), prospects to make progress in this field are good.

5 CONCLUSION

We report new observations with SINFONI and X-Shooter of absorbing-galaxy candidates at $z \sim 1$. The targets have been selected to have a known sky position and an identification based on a proximity argument or based on a photometric or a spectroscopic redshift. We emphasize that this is not a blind search, but a set of eight $z \sim 1$ quasar/absorbing galaxy matched pairs identified by others. Our findings can be summarized as follows.

(i) We report the detection with SINFONI of the Hα emission line of one sub-DLA at $z_{\rm abs} = 0.941\,87$ with $\log N({\rm H\,I}) = 19.38^{+0.10}_{-0.15}$ towards SDSS J002133.27+004300.9 (out of six targets observed). We estimate the SFR to be ${\rm SFR} = 3.6 \pm 2.2\,{\rm M}_{\odot}\,{\rm yr}^{-1}$ in that system. A detailed kinematic study indicates a maximum circular velocity $V_{\rm max} = 80 \pm 40$ km s^{-1} with a dispersion $\sigma = 123 \pm 11$ km s^{-1}. Based on these, we measure a dynamical mass $M_{\rm dyn} = 10^{9.9\pm0.4}\,{\rm M}_{\odot}$ and a halo mass $M_{\rm halo} = 10^{11.9\,\pm\,0.5}\,{\rm M}_{\odot}$. The remaining targets are not detected in our SINFONI observations.

(ii) We report the detection with X-Shooter of the system above as well as one emission line at the redshift $z_{\rm abs} = 0.7402$ of another DLA with $\log N({\rm H\,I}) = 20.4 \pm 0.1$ towards Q0052+0041. The Hα flux in the former system is in perfect agreement with the value derived from the SINFONI observations. The latter system is not detected in Hα but in [O II] as previously reported in the literature from Keck/ESI spectroscopy (Lacy et al. 2003). Based on the detected [O II] flux, we estimate ${\rm SFR} = 5.3 \pm 0.7{\rm M}_{\odot}\,{\rm yr}^{-1}$ in the absorbing galaxy towards Q0052+0041.

(iii) We report the detection of another three objects with X-Shooter at the expected position of the absorbing galaxies in the field of SDSS J011615.51−004334.7, SDSS J122836.8+101841.7 and SDSS J152102.00−000903.1. While these objects are detected in the continuum at NIR wavelengths, a careful visual inspection of the 2D images does not reveal any predominant emission lines for the latter two. The nature and redshift of these objects are therefore not constrained. The former object presents a power-law continuum and an emission line consistent with the redshift of the background quasar, but this could be due in part to contamination from the nearby quasar.

(iv) In two cases (in the field of J045647.17+040052.9 and Q0826−2230), no objects are detected at the expected position of the absorbing galaxies. We note that both these quasars are two orders of magnitude brighter than the other targets in the sample (V mag ~ 16), thus producing a high contrast between the quasar and the faint absorbing galaxy. The former system is also characterized by a small angular separation (impact parameter $b = 0.8$ arcsec).

(v) For all the objects detected in our five-year SINFONI survey, we compute the metallicity difference between the galaxy and the absorbing gas using the underabundance in neutral phase as defined by Lebouteiller et al. (2013): $\delta_{\rm H\,I}(X) = \log(X/{\rm H})_{\rm H\,II} - \log(X/{\rm H})_{\rm H\,I}$. We compare this quantity with the azimuthal angle in the same objects to relate these two independent indicators of gas flows. We find that these quantities do not correlate as expected from simple assumptions. Indeed, some of the gas might fall back on the galaxy as enriched infalling gas. Moreover, multi-phase or clumpy gas might also complicate the simple picture. Additional observations are necessary to relate these two independent probes of gas flows around galaxies.

ACKNOWLEDGEMENTS

We thank Nicolas Bouché, Max Pettini and Crystal Martin for inputs on the work presented here. We also thank the anonymous referee for many suggestions that have improved the paper. We would like to thank the Paranal and Garching staff at ESO for performing the observations in service mode and the instrument team for making a reliable instrument. CP thanks the ESO science visitor programme for support. SQ thanks CNRS and CNES (Centre National d'Etudes Spatiales) for support for his PhD. VPK acknowledges

partial support from the US National Science Foundation grant AST/1108830 and NASA grant NNX14AG74G. Additional support from a NASA/STScI grant for programme 13733 is gratefully acknowledged. This work has been carried out thanks to the support of the OCEVU Labex (ANR-11-LABX-0060) and the A*MIDEX project (ANR-11-IDEX-0001-02) funded by the 'Investissements d'Avenir' French government programme managed by the ANR. L. A. S. acknowledges support from ERC Grant agreement 278594-GasAroundGalaxies.

REFERENCES

Aguirre A., Hernquist L., Schaye J., Weinberg D., Katz N., Gardner J., 2001, ApJ, 560, 599
Bordoloi R. et al., 2011, ApJ, 743, 10
Bouché N. N., Murphy M., Péroux C., Davies R., Eisenhauer F., Forster-Schreiber N., Tacconi L., 2007, ApJ, 669, L5
Bouché N. et al., 2012, MNRAS, 419, 2
Bouché N., Murphy M., Péroux C., Contini T., Martin C., Dessauges-Zavadsky M., 2013, Science, 341, 50
Bouché N., Carfantan H., Schroetter I., Michel-Dansac L., Contini T., 2015, Astrophysics Source Code Library, record ascl:1501.014
Charbrier G., 2003, ApJ, 586L, 133
Cooksey K., Kao M., Simcoe R., O'Meara J., Prochaska J., 2013, ApJ, 763, 37
Cresci G. et al., 2015, ApJ, 799, 82
Dekel A., Silk J., 1986, ApJ, 303, 39
Dessauges-Zavadsky M., Ellison S., Murphy M., 2009, MNRAS, 396, L61
Diamond-Stanic A. M., Coil A. L., Moustakas J., Tremonti C. A., Sell P. H., Mendez A. J., Hickox R. C., Rudnick G. H., 2015, in press
Efstathiou G., 2000, MNRAS, 317, 697
Epinat B. et al., 2009, A&A, 504, 789
Erb D., Shapley A., Pettini M., Steidel C., Reddy N., Adelberger K., 2006, ApJ, 644, 813
Evans C. et al., 2015, preprint (arXiv:e-prints)
Fumagalli M., O'Meara J., Prochaska J., Kanekar N., 2010, MNRAS, 408, 362
Genzel R. et al., 2010, MNRAS, 407, 2091
Goldoni P., Royer F., Francois P., Horrobin M., Blanc G., Vernet J., Modigliani A., Larsen J., 2006, Proc. SPIE, 6269, 2
Jenkins E. B., 2009, ApJ, 700, 1299
Kacprzak G. G. et al., 2014, ApJ, 792, L12
Kelson D., 2003, PASP, 115, 688
Kennicutt R., 1998, ARA&A, 36, 189
Keres D., Katz N., Weinberg D., Davé R., 2005, MNRAS, 363, 2
Lacy M., Becker R. H., Storrie-Lombardi L. J., Gregg M. D., Urrutia T., White R. L., 2003, AJ, 126, 2230
Le Brun V., Bergeron J., Boisse P., Deharveng J., 1997, A&A, 321, 733
Lebouteiller V., Heap S., Hubeny I., Kunth D., 2013, A&A, 553, 16
Lehner N. et al., 2013, ApJ, 770, 138
Martin C., 2005, ApJ, 621, 227
Martin C., Bouché N., 2009, ApJ, 703, 1394
Martin C., Shapley A., Coil A., Kornei K., Bundy K., Weiner B., Noeske K., Schiminovich D., 2012, ApJ, 760, 127
Martin C., Shapley A., Coil A., Kornei K., Murray N., Pancoast A., 2013, ApJ, 770, 41
Meiring J., Lauroesch J., Haberzettel L., Kulkarni V., Péroux C., Khare P., York D., 2011, MNRAS, 410, 2516
Mo H. J., White S. D. M., 2002, MNRAS, 336, 112
Moustakas J., Kennicutt R., Tremonti C., 2006, ApJ, 642, 775
Nelson D., Genel S., Vogelsberger M., Springel V., Sijacki D., Torrey P., Hernquist L., 2015, MNRAS, 448, 59
Ocvirk P., Pichon C., Teyssier R., 2008, MNRAS, 390, 1326
Oppenheimer B., Davé R., 2006, MNRAS, 373, 1265
Pagel B., Edmunds M., Blackwell D., Chun M., Smith G., 1979, MNRAS, 189, 95
Pérez-Montero E., Contini T., 2009, MNRAS, 398, 949
Péroux C., Bouché N., Kulkarni V., York D., Vladilo G., 2011a, MNRAS, 410, 2237
Péroux C., Bouché N., Kulkarni V., York D., Vladilo G., 2011b, MNRAS, 410, 2251
Péroux C., Bouché N., Kulkarni V., York D., Vladilo G., 2012, MNRAS, 419, 3060
Péroux C., Bouché N., Kulkarni V., York D., 2013, MNRAS, 436, 2650
Pettini M., 2003, Cosmochemistry: The Melting Pot of Elements. Cambridge Univ. Press, New York
Pettini M., Pagel B., 2004, MNRAS, 348, 59
Pettini M., Smith L., Hunstead R., King D., 1994, ApJ, 426, 79
Pettini M., Shapley A., Steidel C., Cuby J., Dickinson M., Moorwood A., Adelberger K., Giavalisco M., 2001, ApJ, 554, 981
Pieri M., Martel H., Grenon C., 2007, ApJ, 658, 36
Queyrel J. et al., 2012, A&A, 539, 93
Rahmati A., Schaye J., 2014, MNRAS, 438, 529
Rahmati A., Pawlik A. H., Raičevic M., Schaye J., 2013, MNRAS, 430, 2427
Rao S., Turnshek D., Nestor D., 2006, AJ, 636, 610
Rao S., Belfort-Mihalyi M., Turnshek D., Monier E., Nestor D., Quider A., 2011, MNRAS, 416, 1215
Retzlaff J. et al., 2014, Proc. SPIE, 9149, 914903
Rudie G. et al., 2012, ApJ, 750, 67
Rupke D., Veilleux S., Sanders D., 2005, ApJS, 160, 115
Ryan-Weber E., Pettini M., Madau P., Zych B., 2009, MNRAS, 395, 1476
Sato T., Martin C., Noeske K., Koo D., Lotz J., 2009, ApJ, 696, 214
Schaye J. et al., 2010, MNRAS, 402, 1536
Schroetter I., Bouché N., Péroux C., Murphy M., Contini T., Finley H., 2015, ApJ, 804, 83
Shapley A., Steidel C., Pettini M., Adelberger K., 2003, ApJ, 588, 65
Shull J. M., 2014, ApJ, 784, 142
Shull J., Danforth C., Tilton E., 2014, ApJ, 796, 49
Som D., Kulkarni V., Meiring J., York D., Péroux C., Lauroesch J., Aller M., Khare P., 2015, ApJ, 806, 25
Steidel C., Sargent W., 1992, ApJS, 80, 1
Steidel C., Pettini M., Hamilton D., 1995, AJ, 110, 2519
Steidel C., Pettini M., Adelberger K., 2001, ApJ, 546, 665
Steidel C., Erb D., Shapley A., Pettini M., Reddy N., Bogosavljevic M., Rudie G., Rakic O., 2010, ApJ, 717, 289
Steidel C., Bogosavlejevic M., Shapley A., Kollmeier J., Reddy N., Erb D., Pettini M., 2011, ApJ, 736, 160
Stewart K., Kaufmann T., Bullock J., Barton E., Maller A., Biemand J., Wadsley J., 2011, ApJ, 738, 39
Stinson G. et al., 2012, MNRAS, 425, 1270
Swinbank A. M., Sobral D., Smail I., Geach J. E., Best P. N., McCarthy I. G., Crain R. A., Theuns T., 2012, MNRAS, 426, 935
Takamiya M., Chun M., Kulkarni V. P., Gharanfoli S., 2012, AJ, 144, 111
Tremonti C., Moustakas J., Diamond-Stanic A., 2007, ApJ, 663, 77
Tumlinson J. et al., 2011, ApJ, 733, 111
van de Voort F., Schaye J., 2012, MNRAS, 423, 2991
van Dokkum P., 2001, PASP, 113, 1420
Veilleux S., Cecil G., Bland-Hawthorn J., 2005, ARA&A, 43, 769
Vernet J. et al., 2011, A&A, 536, 105
Weiner B. et al., 2009, ApJ, 692, 187
Werk J., Prochaska J., Thom C., Tumlinson J., Tripp T., O'Meara J., Peeples M., 2013, ApJS, 204, 17
Wilkinson M. I., Evans N. W., 1999, MNRAS, 310, 645
Zafar T., Péroux C., Popping A., Milliard B., Deharveng J., Frank S., 2013, A&A, 556, 141

This paper has been typeset from a TEX/LATEX file prepared by the author.